Int. J. Electrochem. Sci., 15 **(2020)** 4161 – 4178, doi: 10.20964/2020.05.47

International Journal of
ELECTROCHEMICAL
SCIENCE
www.electrochemsci.org

Microstructure and Corrosion Behavior of as-cast 90Cu-10Ni Alloys with Different Yttrium Content

Yinghui Zhang[1], *Chunmei Song*[1], *Yanfeng Cao*[1], *Hang Wang*[2], *Zhigang Wang*[1,*], *Bin Yang*[1,*]

[1] School of Material Science and Engineering, Jiangxi University of Science and Technology, Ganzhou 341000, China
[2] Institute of Engineering and Research, Jiangxi University of Science and Technology, Ganzhou 341000, China
[*]E-mail: wzgang2008cn@163.com , yangbin65@126.com

Received: 13 January 2020 / *Accepted:* 12 February 2020 / *Published:* 10 April 2020

The microstructure and corrosion behavior of 90Cu–10Ni alloys with different contents of the rare earth (RE) element yttrium (Y) were investigated using electron probe micro analysis (EPMA), scanning electronic microscopy (SEM), X-ray diffraction (XRD), X-ray photoelectron spectroscopy (XPS), and electrochemical impedance spectroscopy (EIS). The results showed that proper amount of Y could refine the secondary dendrite spacing of the as-cast microstructure. As the Y content increased, the number and sizes of the yttrium-rich oxysulfide inclusions increased. Meanwhile, the corrosion resistance of the alloys in a 3.5% NaCl solution immersed for 30 d improved first and then deteriorated with the increase in the Y content. When the Y content was 0.021%, the resistance of the inner film was greater than 1500 kΩ. This was attributed to the inhibitory effect of Y on the transformation from Cu_2O to $Cu_2(OH)_3Cl$ and the influence of Y on the diffusion of Ni.

Keywords: 90Cu-10Ni alloy; rare earth Y; as-cast microstructure; corrosion resistance; XPS

1. INTRODUCTION

The exploitation of offshore energy resources and development of marine economies are growing trends due to the abundant natural resources in the ocean [1]. The working environment of marine engineering materials is extremely complex, due in part to the corrosion of materials [2–4]. Cu–Ni alloys are considered to be very important commercial alloys in marine environments. The corrosion behaviors of Cu–Ni alloys in solutions containing chloride ions have been investigated by many authors [5–9]. An important approach to improve the corrosion resistance of Cu-Ni alloys is to modify the alloy composition.

In a simulated seawater environment, immersion experiments have revealed that rare earth elements have remarkable effects on the microstructures and corrosion behaviors of Cu–Ni alloys [10–14]. Dong et al. [13] reported that the as-cast structure of the Cu-15Ni alloy changed from typical dendrites to fine equiaxed grains when the rare earth content was 0.05%–0.08%. Mao et al. [10] showed that rare earth elements significantly affected the dendrite structure refinement, grain size, and purifying alloy melt of the Cu-30Ni alloy. The oxide films on the surfaces of copper–nickel alloys are the key to their corrosion resistances, and the addition of rare earth elements can ensure the connection of the oxide film and the matrix, improving the corrosion resistance [14]. North and Pryor suggested that the semiconductivity of a Cu_2O film that formed on the Cu-Ni alloy caused the nickel ions to occupy cationic vacancies in the Cu_2O film and annihilate electron vacancies, thereby improving the corrosion resistance of the alloy [15]. Ma et al. [16] found that a Cu_2O film formed by the deposition of dissolved copper species first, after which it transformed by an internal oxidation mechanism. Meanwhile, Efird [17] explained that NiO formed in the interface between the based alloy and the film by a passivation mechanism and protected the matrix from further corrosion. Some researchers have studied the effects of rare earth elements on the corrosion behaviors of copper alloys. Dong et al. [13] observed that the corrosion resistance of the Cu-15Ni alloy was greatly improved by adding the proper amount of rare earth elements, whereas the excess addition of rare earth elements worsened the corrosion resistance. Li and co-workers [18] indicated that the corrosion resistance of cast pure copper was improved significantly when the Ce content was 0.069 wt% due to the formation of a compact oxide film. Liu [12] studied the corrosion resistance of Cu–Ni–Fe alloys and found that the bonding force between the alloy matrix and the oxide film was increased due to the addition of La. Thus, the roles of rare earth elements in Cu-Ni alloys have been studied in depth. However, no systematic study on the effect and mechanisms of rare earth elements on the corrosion resistance of the 90Cu–10Ni alloy in NaCl solution has been conducted.

It has been reported that processing conditions affect the distribution of yttrium (Y)-based inclusions [19], and different forms of deformation have a significant impact on the corrosion resistance of the 90Cu–10Ni alloy [20]. To avoid the effect of subsequent deformation on the microstructures and corrosion resistances of the alloys, as-cast alloys were selected to investigate the effect of the rare earth element Y on the microstructure and corrosion resistance of the 90Cu-10Ni alloy. The role of rare earth elements in the formation mechanism of corrosion product films formed after one month of immersion in 3.5% NaCl solution is preliminarily discussed in this paper.

2. EXPERIMENTAL

2.1 Materials and solution

The as-cast 90Cu–10Ni alloy with different rare earth contents was melted in a vacuum induction furnace under an argon atmosphere. According to the preliminary experimental research, a suitable rare earth contents gradient were designed. When the temperature of copper-nickel alloy reaches 1300 ℃ the Yttrium additive was added into it. Then cooled the molten metal down to 1250 ℃

after stirring and poured into a preheated metal mold with a size of 20mm×80mm×160mm after placed statically for 10 min. Finally, the samples were cooled to room temperature. The actual Y contents and other chemical compositions of the alloys were determined and are listed in Table 1.

Table 1. Compositions (wt%) of experimental 90Cu–10Ni alloy

Sample	Cu	Ni	Fe	Mn	Y	S	C
S1	Bal.	11.58	1.88	1.02	0	0.0010	0.0035
S2	Bal.	11.43	1.63	0.96	0.0039	0.0010	0.0084
S3	Bal.	11.44	1.61	0.96	0.021	0.0010	0.0084
S4	Bal.	11.58	1.67	0.96	0.053	0.0012	0.0084

The specimens cut from the ingot were polished through a series of SiC papers as well as 2.5 and 0.5 μm diamond grinding paste, followed by washing with deionized water and ethanol and etching with an aqueous solution of $Fe(NO_3)_3$ and hydrochloric acid. The microstructures were observed by optical microscopy (OM, Zeiss 2550). The morphology and distribution of the rare earth inclusions were characterized by electron probe micro-analysis (EPMA, Shimadzu model 1610).

2.2 Characterization of corrosion products

2.2.1 SEM morphology observations

The surface morphologies of the corrosion product films formed on the specimens after 30 d of immersion in a 3.5 wt.% NaCl solution were observed by scanning electron microscopy (SEM, ZEISS Sigma) with accelerating voltage of 10 kV. Before SEM observed, the samples were adhered to a layer of conductive adhesive on its surface in order to enhance the conductivity of the corrosion product film.

2.2.2 XRD analysis

X-ray diffraction (XRD, Empyrean) was used to analyze the phase components of the corrosion products with a 2.0°/min scanning speed and a 10–90° 2θ range. The obtained diffraction spectra were analyzed using the commercial software Jade 6.

2.2.3 XPS analysis

The profile composition of corrosion product film was analyzed by an X-ray photoelectron spectroscopy (XPS, VG ESCALAB 250) argon ion sputtering. After sputtering, the variation of Cu, O, Cl and Ni contents with sputtering depth was analyzed and the sputtering rate was about 0.2 nm s^{-1} (vs.

Ta_2O_5). The Cu 2p and Ni 2p spectra were analyzed by deconvolution fitting using the XPSPEAK1 software.

2.2.4 Electrochemical measurements

The specimens with a dimension of 10mm×10mm×3mm were cut from the 90Cu–10Ni alloy to make electrodes. The corrosion experiment of the alloys was carried out in a 3.5% NaCl solution in a constant temperature environment using Parstat 4000A electrochemical workstation. The measurements were conducted using a standard three-electrode cell, where a saturated calomel electrode (SCE) was used as the reference electrode, a platinum electrode was used as the counter electrode, and the sample with an exposed area of 1 cm^2 was used as the working electrode.

3. RESULTS

3.1 Effects of Y contents on microstructure

3.1.1 Effect of Y on morphology and distribution of inclusions

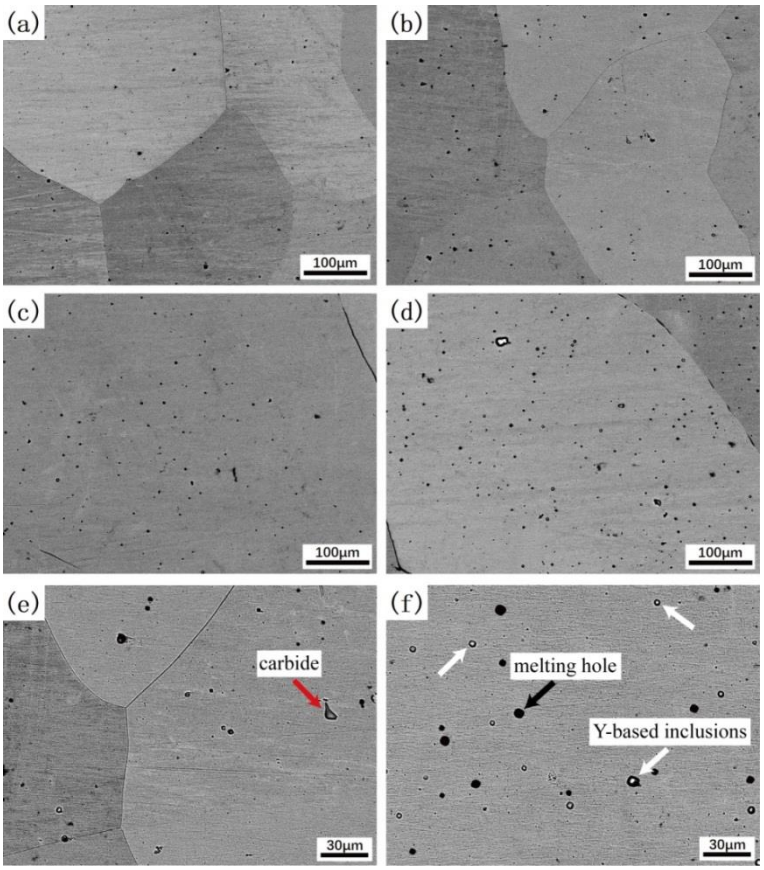

Figure 1. EPMA image of inclusions in 90Cu–10Ni alloy: (a)S1:0%Y, (b) S2:0.0039%Y, (c) S3:0.021%Y, (d) S4:0.053%Y, (e) magnified image of S2, and (f) magnified image of S4.

Y is a typical heavy rare earth (RE) element, with a high active chemical energy, and it easily reacts with O and S during solidification to form RE-O-S complex inclusions [19,21]. The morphology and sizes of rare earth inclusions on the as-cast 90Cu–10Ni alloy after homogenization annealing were analyzed by EPMA, as shown in Fig. 1. As shown in Fig. 1(a) black melting holes formed during melting in the rare-earth-free sample S1.

As shown in Fig. 1(b)–(d), as the Y content increased, the number and sizes of the rare earth inclusions in the black melt holes increased, and the sizes of the inclusions ranged from the sub-micron scale to the micron scale. Two kinds of inclusions were evident in the magnified image of the S3 and S4 samples, as shown in Fig. 1(e) and (f). The triangular black–gray inclusions in Fig. 1(e) are carbides or other impurities [19] (red arrows). From Fig. 1(f), it is evident that there were spherical bright white inclusions (white arrows) in some of the black melt holes but there were no inclusions in others (black arrows), which may have been due to the inclusions falling off during the sample preparation. Fig. 2 indicates that the bright white Y-based inclusions in the melt holes consisted mainly of yttrium oxysulfide.

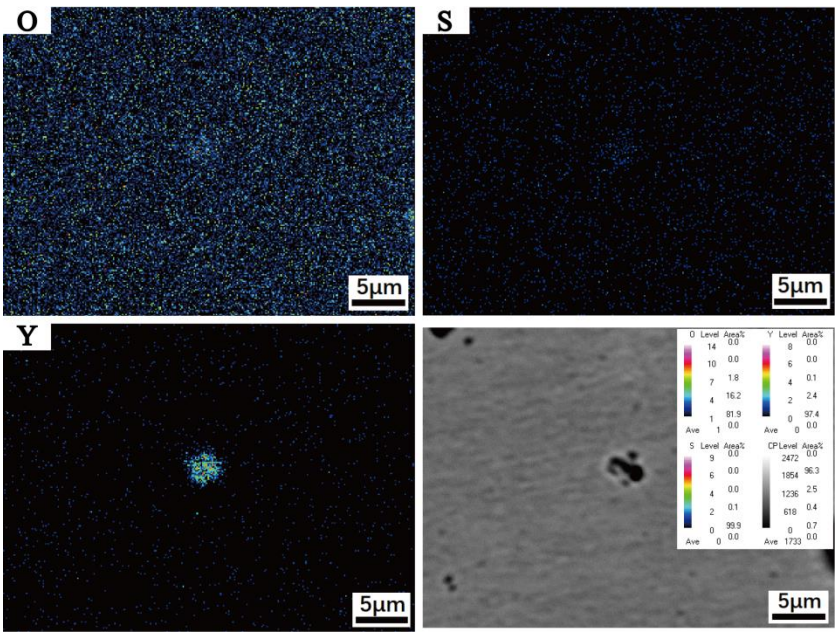

Figure 2. EPMA surface scanning results of rare earth inclusion in the S4 sample.

3.1.2 Effect of Y on microstructure

The as-cast microstructure of the 90Cu–10Ni alloy is typical dendritic, as shown in Fig. 3. The secondary dendrite spacings of the alloys with different Y contents were different. The numbers of secondary dendrites for the different Y-content alloys were calculated using the Image-Pro software over a certain length range (300 μm). The greater the secondary dendrite number was, the smaller the dendrite spacing was. As shown in Fig. 4, the secondary dendrite spacing of the rare-earth-free S1 sample was significantly larger than that of other rare-earth-containing alloys, indicating that the Y

could effectively refine the secondary dendrite spacing [22]. With the increase in the Y content, the secondary dendrite spacing decreased first and then increased slightly, and the S3 sample with a Y content of 0.021% had the smallest secondary dendrite spacing.

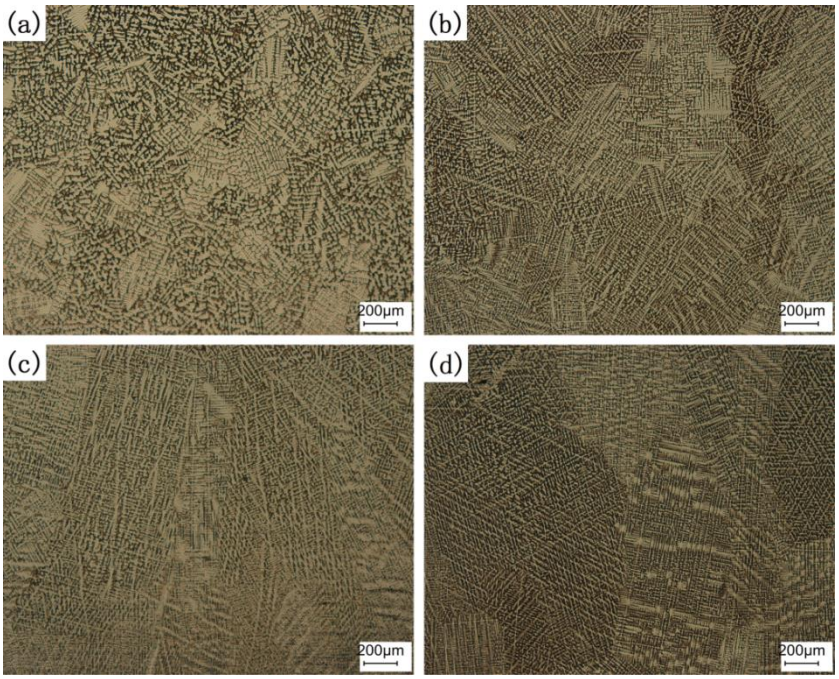

Figure 3. As-cast structures of 90Cu–10Ni alloys with different Y contents: (a) S1:0%Y, (b) S2:0.0039%Y, (c) S3:0.021%Y, and (d) S4:0.053%Y.

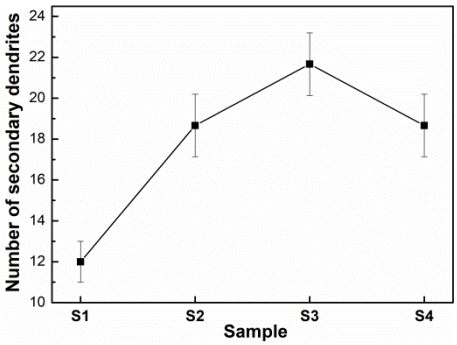

Figure 4. Statistical result of the number of secondary dendrites.

3.2 Effects of Y contents on morphologies of corrosion products

The macroscopic corrosion morphologies of the 90Cu–10Ni alloys with different Y contents after immersion in a 3.5% NaCl solution for 30 d are shown in Fig. 5. As the Y content increased, the colors of the corrosion products became darker, and blue corrosion product particles even appeared on the surface of the S4 sample, which may have been atacamite that transformed from Cu_2O.

The microscopic morphologies of the corrosion products on the surfaces of the 90Cu–10Ni alloys are presented in Fig. 6. Local shedding of the film occurred at the edge (the area indicated in Fig. 5) of the alloys S1, S2, and S4, which exposed the matrix. However, the film on the surface of the S3 alloy did not fall off, which indicated that the corrosion product layer of the S3 alloy was closely bound to the matrix. Meanwhile, the corrosion morphologies of the cores of the samples in the upper right corner of Fig. 6 show that a layer of the corrosion products consisted of larger clastic particles with higher porosities on the surface of the S1 alloy, with poor compactness and no protection. However, for the samples with added Y, the clastic particles were finer, and the porosity was greatly reduced. In particular, the corrosion products on the surface of the S3 alloy were the most compact, and the porosity was the lowest.

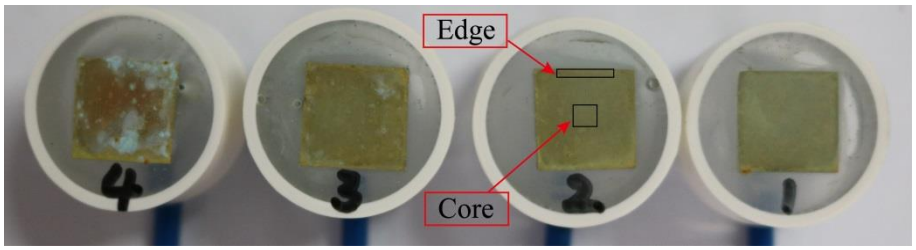

Figure 5. Macroscopic morphologies of the corrosion products formed on the 90Cu–10Ni alloys after 30 d of immersion in a 3.5% NaCl solution.

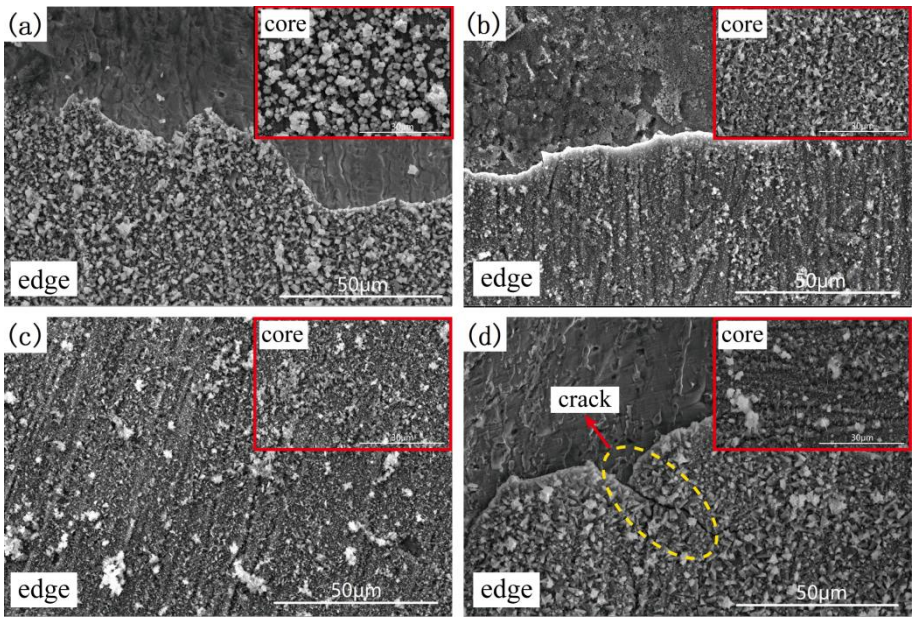

Figure 6. SEM morphologies of the corrosion products formed on the 90Cu–10Ni alloys after 30 d of immersion in a 3.5% NaCl solution: (a)S1:0%Y, (b)S2:0.0039%Y, (c)S3:0.021%Y, and (d)S4:0.053%Y.

Reducing the porosity of the surface film effectively prevented chloride ions from attacking the inner film, which could better protect the matrix [23]. The corrosion products on the surface of the S4

alloy formed evident cracks, as shown in Fig. 6(d), which may have led to peeling of the film [24]. The results indicated that the rare earth content of the S4 alloy was excessive.

3.3 Effect of Y content on compositions of corrosion products

3.3.1 XRD analysis for corrosion products

The XRD patterns of the corrosion products that formed on the alloys after 30 d of immersion in the 3.5% NaCl solution are presented in Fig. 7. The results indicated the presence of crystalline Cu, $Cu_2(OH)_3Cl$, and Cu_2O in the corrosion products. In addition to the Cu peak, $Cu_2(OH)_3Cl$ was the main peak, whereas the Cu_2O peak was very weak for the corrosion products of the S1 sample. However, for the other three samples with added Y, the Cu_2O peak was relatively strong. Based on the XRD and SEM analysis of the corrosion products, the larger clastic particles on the surface of the S1 sample were $Cu_2(OH)_3Cl$. Thus, the rare earth Y could effectively inhibit the transformation of Cu_2O to $Cu_2(OH)_3Cl$ during corrosive chemical reactions, which may have been due to the inhibiting effect of Y on the diffusion of Cl^-.

The strong Cu peak in the corrosion product film was detected by XRD. There are two possibilities for the existence of Cu peak: one was derived from the alloy matrix under the corrosion products, because copper was the main element in the 90Cu–10Ni alloy. And the other was derived from the corrosion product layer, which reprecipitated from the dissolved Cu species by the reduction of Cu^{2+} to Cu during the corrosion reaction [17,25,26].

The XRD pattern showed that atacamite ($Cu_2(OH)_3Cl$) was present in the form of two polymorphs: paratacamite and botallackite [27–29]. The difference between the two polymorphs was that the free energy of formation for botallackite was lower than that of paratacamite, and the stability of botallackite was worse than that of paratacamite. Thus, botallackite was first formed in the chemical reaction process and was finally transformed into stable paratacamite due to the substitution of Ni^{2+} at some Cu^{2+} sites [27,30]. It has been reported that the Ni compounds are barely detectable by XRD in corrosion products [15,25,31]. However, based on the presence of paratacamite in the film, it was inferred that nickel–iron as existed as a dopant in the corrosion products. The effect of Y on Ni diffusion will be discussed later.

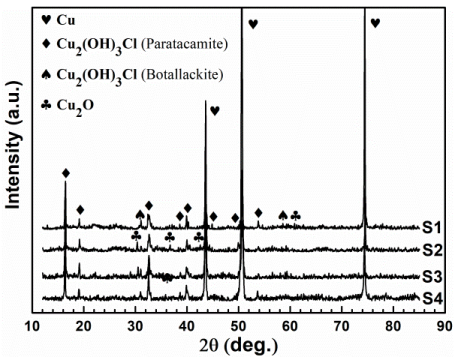

Figure 7. XRD profile of the corrosion products formed on the 90Cu–10Ni alloy after 30 d of immersion in a 3.5% NaCl solution.

3.3.2 XPS analysis for corrosion products

XPS was used to analyze the profile compositions of the corrosion product films of the alloys with 0.021% Y and no Y after immersion in a 3.5% NaCl solution for 30 d. For the range of sputtering depths from 0 to 200 nm, the depth profiles of the main elements in the films are shown in Fig. 8. Compared with the sample without Y, the Ni content in the film was higher when the rare earth content was 0.021%, which indicated that Y may be beneficial to the diffusion of Ni. Meanwhile, the Ni content in the film increased with the sputtering depth, which indicated that the enrichment of Ni was mainly in the inner layer of the film.

The Cu 2p spectra of the corrosion product film corresponding to sputtering depths of 0 and 200 nm are displayed in Fig. 9. The spectra for the sample with a sputtering depth of 0 nm showed that there were very strong Cu 2p3/2 peaks at binding energies (BEs) of ~935 and ~955 eV with shake-up features at ~942.2 and ~963 eV, which indicated that the chemical state of Cu element in the outermost layer was Cu^{2+}. This was evidence of the existence of atacamite ($Cu_2(OH)_3Cl$) [32], which agrees with the XRD results in Fig. 7.

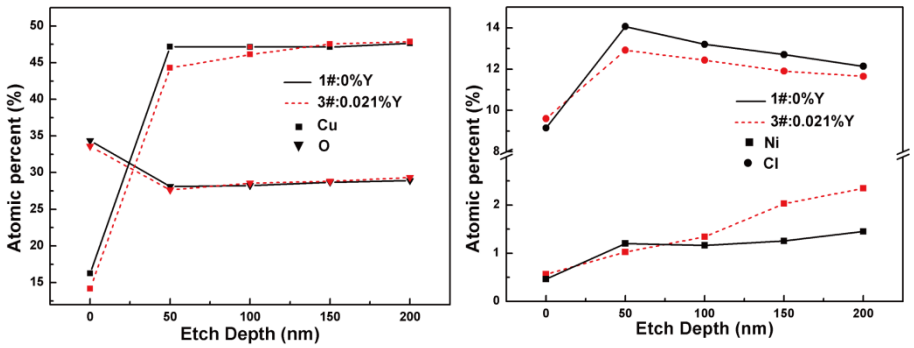

Figure 8. Depth profiles of the elements sputtered at the surfaces of the corrosion products formed on the 90Cu–10Ni alloy after 30 d of immersion in a 3.5% NaCl solution.

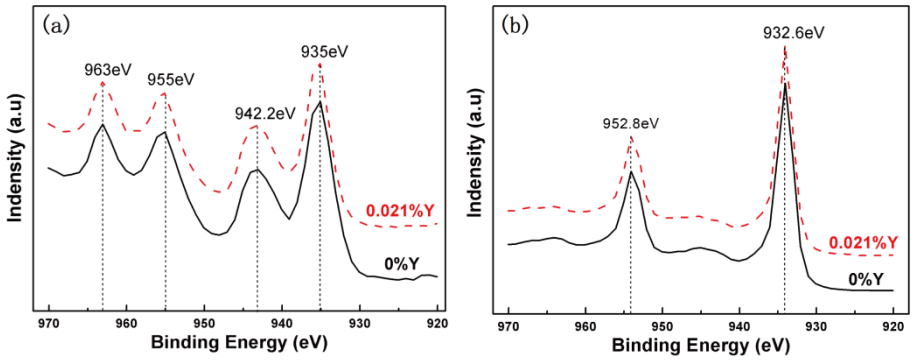

Figure 9. XPS Cu 2p spectra for the corrosion product films formed on the 90Cu–10Ni alloy after 30 d of immersion in a 3.5% NaCl solution for sputtering depths of (a) 0 nm and (b) 200 nm.

No shake-up peak was detected in the Cu 2p spectra after 200-nm sputtering, and only Cu_2O or Cu peaks were identified in the BEs of ~932.6 and ~952.8 eV. The XRD and XPS results indicated

that the chemical state of Cu was Cu(II) at the outermost layer of the film, whereas that in the middle layer was Cu(I).

The Ni 2p spectra for sputtering depths of 0 and 200 nm are presented in Fig. 10. During the peak deconvolution and fitting for the Ni 2p, the double nature of Ni 2p lines was taken into account, and the lines were fitted with similar intensity ratio, width and binding energy separation of ~6 eV[17,33]. The deconvolution results for the 0- and 200-nm sputtering depths showed the same with three peaks: a peak centered at BE of ~852.7 eV with a shake-up peak at ~858.4 eV, a peak centered at BE of ~855.6 eV with a shake-up peak at ~861.1 eV, and a peak centered at BE of ~856.9 eV with a shake-up peak at ~863.2 eV, which were assigned to metallic Ni, NiO, and $Ni(OH)_2$, respectively [33]. The Ni 2p spectra showed that the intensity of the peak at the 200-nm sputtering depth (Fig. 10(c), (d)) was stronger than that at the 0-nm sputtering depth (Fig. 10(a), (b)), which indicated that the Ni contents in the film increased as the sputtering proceeded.

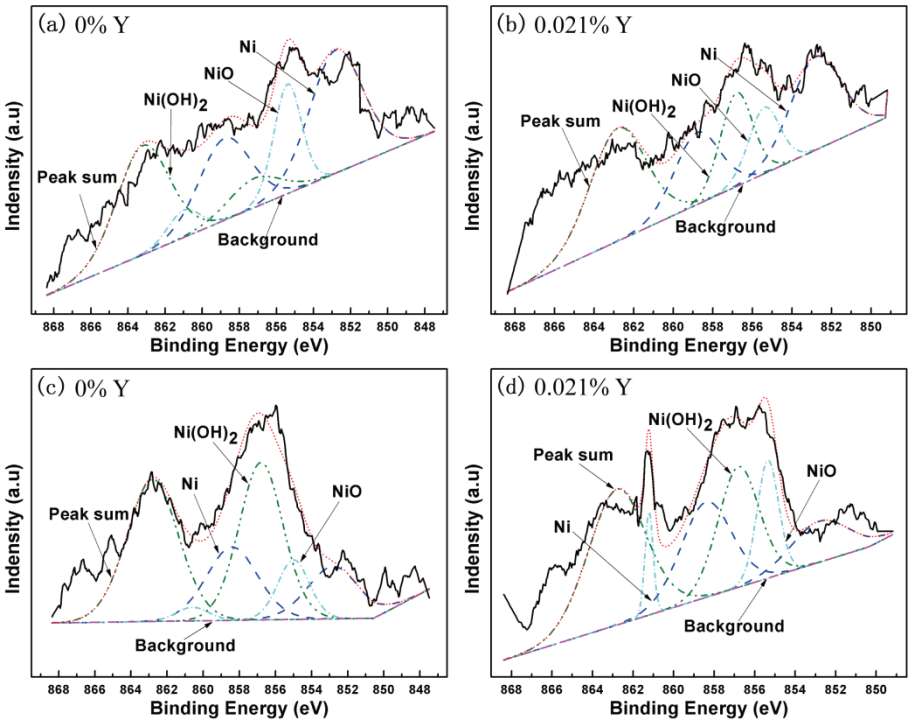

Figure 10. XPS Ni 2p spectra with different Y contents for the corrosion product film formed on the 90Cu–10Ni alloy immersed in a 3.5% NaCl solution for 30 d for sputtering depths of (a), (b)0 nm and (c), (d)200 nm.

3.4 EIS analysis for corrosion products

EIS was used to characterize the corrosion resistances of the samples with immersion time of 0d, 3d, 15d and 30d respectively to study the effect of the Y contents on the resistance of the corrosion product film. The Nyquist plots of the samples immersed for 0d in Fig. 11(a) showed that in addition to the capacitive loops in the high-frequency range, Warburg diffusion impedance occurred in the low-frequency range when the samples were initially exposed to the 3.5% NaCl solution. This can be

explained as follows: there was no film or a thin film present in the initial stage of immersion, and various ions directly or easily contacted the matrix through the corrosion product film. Thus, the electrochemical reaction was controlled by charge transfer and dissolved oxygen diffusion processes. However, the Warburg impedance disappeared, and the diameters of the capacitive loops increased dramatically for the samples immersed for 3d, 15d and 30d in the 3.5% NaCl solution. This is because the corrosion product film was formed on the alloy surface, which played a protective role on the alloy, and the diffusion process was hindered, resulting in the electrochemical reaction of the alloy was mainly controlled by the charge transfer process. In addition, only one maximum peak angle could be identified in the phase angle plots for the samples immersed for 0d as shown in Fig. 11(b).

As shown in Fig. 11(c), when the samples were immersed for 3d, the diameter of the capacitive loop of S3 sample with Y content of 0.021% was significantly larger than that of the other three samples. The Bode plots in Fig. 11(d) showed that the total impedance magnitudes of S3 sample at the lower frequency range is the largest. In the phase angle plots there were two maximum peak angles in the samples containing Y, while there was only one maximum peak angle in the sample without Y. This was related to the formation of "double layer film" structure on the alloy surface, which indicates that rare earth Y promoted the formation of protective corrosion product film [34,35]. As shown in Fig. 11(e), when the samples were immersed for 15d, the diameters of the capacitive loops of the samples containing Y were far greater than that of the sample without Y. Bode plots in Fig. 11(f) showed that the total impedance magnitudes of the samples containing Y in the lower frequency range were larger than that of S1 sample without Y. As shown in Fig. 11(g), the diameters of the capacitive loops of the samples immersed for 30d increased with the increased in the Y content to 0.021% and decreased when the Y content was 0.053%.

The impedance spectra were fitted to an equivalent circuit to obtain the corresponding impedance parameters reflecting the effect of Y on the corrosion resistances of the alloys. The equivalent circuits in Fig. 12(a) and (b) were used to describe the structures of the samples immersed for 0d and immersed for 3d, 15d, 30d, respectively [16,36,37]. In the equivalent circuit, R_s represents solution resistance, C_{ct} represents the capacitance of the double electric layer and R_{ct} represents charge transfer resistance between the alloy substrate and solution. In particular, Q_{ct} was used instead of C_{ct} in Fig. 12(b) because of the formation of an uneven film, and the electric double layer could no longer be represented by an ideal capacitive element[38]. Q_1 and R_{f1} are defined as the film capacitance and film resistance of the initial oxide film or the outer film respectively [39]. Q_2 and R_{f2} are the parameters describing the capacitance and resistance of the inner corrosion product film, respectively [16,24]. According to the characteristics of Nyquist plots, the Warburg impedance was introduced in Fig. 12(a) to represent the diffusion process. The quality of the fitting was judged by the Chi-squared (χ^2) value [40], and the fitting parameters are listed in Table 2 and Table 3.

As shown in Table 2, for the samples immersed in 3.5% NaCl solution for 0d, the charge transfer resistance (R_{ct}) and film resistance (R_{f1}) of the alloys with Y were larger than those of the alloy without Y, which indicated that the addition of Y could reduce the corrosion rate of the 90Cu–10Ni alloy.

For the samples immersed in 3.5% NaCl solution for 3d, 15d and 30d, the resistance of the inner layer (R_{f2}) was much greater than the resistance of the outer layer (R_{f1}) as shown in Table 3. In

addition, when the samples were immersed for 30d, the capacitance (Q_2) of the inner layer was one order of magnitude smaller than the capacitance (Q_1) of the outer layer, indicating that the inner layer was more compact and thus more protective than the outer layer[16]. Meanwhile, with the increase of immersion time, the resistance of inner layer (R_{f2}) increased obviously.

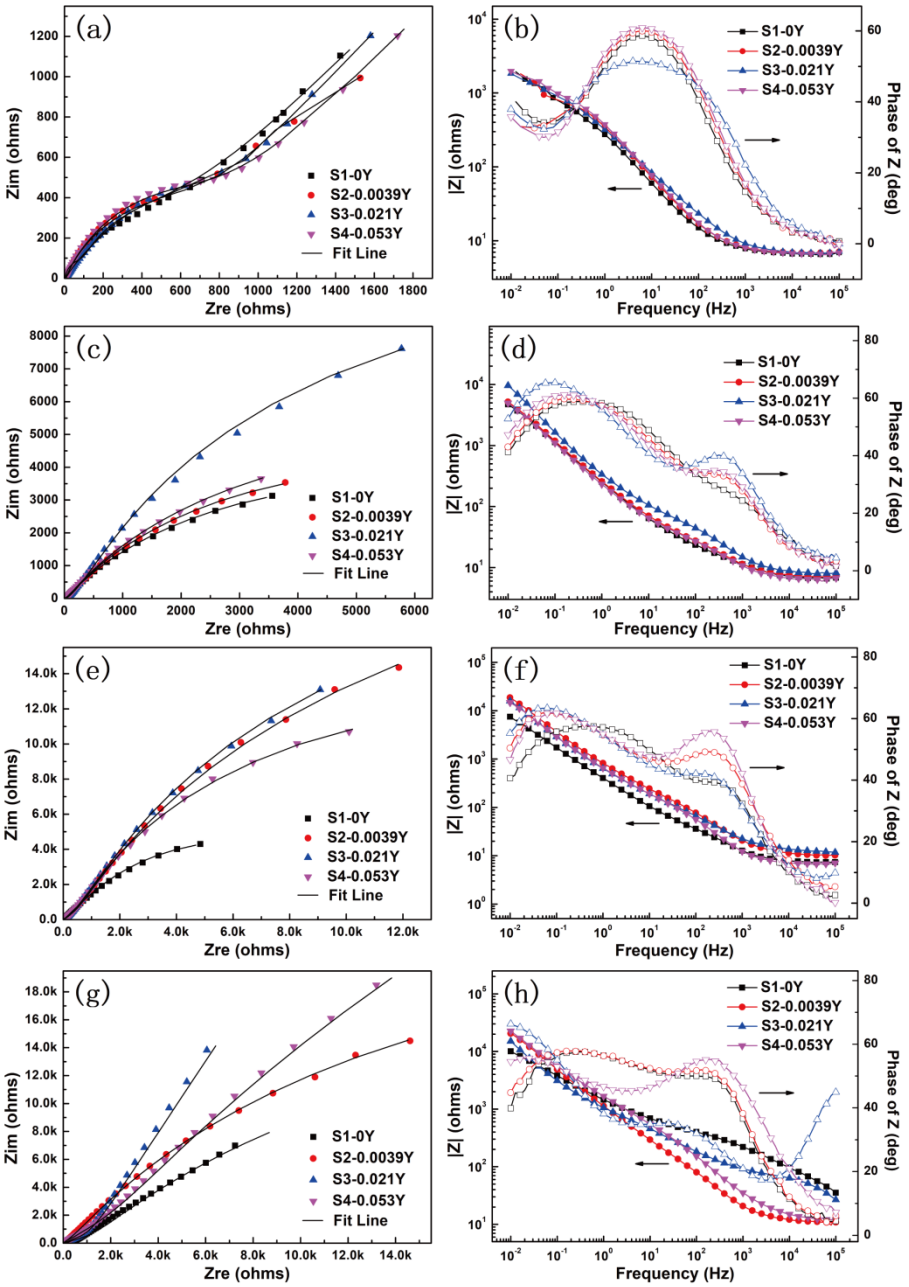

Figure 11. Nyquist and Bode plots of 90Cu-10Ni alloy with different rare earth contents after 0d, 3d, 15d, 30d immersion in 3.5% NaCl solution:(a)、(b)0d；(c)、(d)3d；(e)、(f)15d；(g)、(h)30d

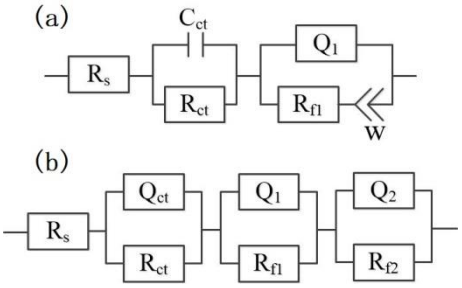

Figure 12. Equivalent circuits used for fitting the impedance spectra of the 90Cu–10Ni alloys with different rare earth contents after (a) 0 d and (b) 3d, 15d, 30d of immersion in the 3.5% NaCl solution

There were significant differences in the resistance of inner film (R_{f2}) with different Y contents for the samples immersed 30d, especially for the S3 sample. Its R_{f2} was the largest—one order of magnitude larger than that of the S4 sample—and even two orders larger than that of the rare-earth-free sample. This is compelling evidence that the corrosion resistance of the 90Cu–10Ni alloy can be greatly improved by adding the proper amount of Y.

Table 2. Circuit parameters fitted from the EIS results for 0d after immersion in 3.5% NaCl solution

Samples	R_s /Ω·cm^2	$C_{ct}\times10^{-3}$ /F·cm^{-2}	$W\times10^{-3}$ /Ω^{-1}cm^{-2}s$^{-0.5}$	R_{ct} /Ω·cm^2	$Q_1\times10^{-4}$ /F·cm^{-2}	n_1	R_{f1} /Ω·cm^2	R_{total} /Ω·cm^2	$\chi^2\times10^{-4}$
0Y	5.760	2.387	2.303	170.6	5.161	1.0000	252.4	423	7.367
0.0039Y	6.844	1.545	1.015	197.5	6.590	0.7412	372	570	9.346
0.021Y	6.600	0.974	2.063	240.6	7.481	0.6649	440	681	9.030
0.053Y	6.678	2.254	2.239	190.3	6.367	0.7440	668	858	9.441

Table 3. Circuit parameters fitted from the EIS results for 3d, 15d, 30d after immersion in 3.5% NaCl solution

Time	Samples	R_s /Ω·cm^2	$Q_{ct}\times10^{-4}$ /F·cm^{-2}	n_{ct}	R_{ct} /Ω·cm^2	$Q_1\times10^{-4}$ /F·cm^{-2}	n_1	R_{f1} /Ω·cm^2	$Q_2\times10^{-4}$ /F·cm^{-2}	n_2	R_{f2} /Ω·cm^2	R_{total} /Ω·cm^2	$\chi^2\times10^{-4}$
3d	0Y	6.411	5.524	0.6753	11.12	5.502	0.6723	20.8	10.54	0.7104	11050	11082	6.430
	0.0039Y	6.884	3.201	0.8253	11.90	3.743	0.5696	5369	11.55	0.7417	11800	17181	5.617
	0.021Y	7.465	2.277	0.8526	28.94	1.570	0.5463	9288	15.95	0.8000	15650	24967	8.070
	0.053Y	6.277	2.512	0.7824	16.64	3.569	0.6503	3167	12.56	0.7394	14130	17314	6.071
15d	0Y	6.980	3.185	0.9241	11.39	8.977	0.9996	2587	6.484	0.6196	14540	17138	6.659
	0.0039Y	9.653	1.998	0.8898	23.92	8.691	0.6103	444.4	4.046	0.7927	52680	53148	4.357
	0.021Y	11.15	1.384	0.7429	32.52	10.34	0.9207	28200	4.119	0.5480	49110	77343	9.281
	0.053Y	6.596	1.081	0.8675	76.54	6.722	0.7071	511.6	5.435	0.8397	30650	31238	6.270
30d	0Y	12.04	1.735	0.9972	15.22	6.055	0.4667	985	0.6389	0.6227	53180	54180	1.073
	0.0039Y	10.52	0.803	0.9963	22.78	4.447	0.6568	998.6	0.5645	0.7100	58020	59041	3.731
	0.021Y	5.23	0.453	0.8580	52.67	2.975	0.5217	1071	0.2790	0.7748	1634000	1635124	5.169
	0.053Y	11.09	0.776	0.8529	168	4.622	0.6170	1465	0.2916	0.7131	163200	164833	4.827

4. DISCUSSION

4.1 Formation mechanism of Cu_2O film

The double-layer structure of the corrosion product film formed on copper–nickel alloy by immersion in natural seawater or a NaCl solution has been reported by many researchers [15,16,41]. The outer layer of the Cu_2O film is formed by reprecipitation from the dissolved copper species ($CuCl_2^-$) [36]. However, after a period of immersion, the film becomes thick and compact, and the generation of $CuCl_2^-$ from the dissolution of metallic Cu is inhibited. Therefore, the formation mechanism of the inner Cu_2O film is transformed into inward oxidation, which is directly oxidized from metal Cu to Cu_2O.

At the beginning of the immersion in a 3.5% NaCl solution, the copper matrix in direct contact with the solution is dissolved and reacts with Cl^- to form $CuCl_2^-$, which is the main anodic reaction process of copper alloy in a NaCl solution [42,43]. The chemical reaction is carried out by the equations (1) - (3):

$$Cu \leftrightarrow Cu^+ + e^-, \quad (1)$$

$$Cu^+ + Cl^- \leftrightarrow CuCl, \quad (2)$$

$$CuCl + Cl^- \leftrightarrow CuCl_2^-, \quad (3)$$

The main cathodic reaction is shown in equation (4):

$$O_2 + 2H_2O + 4e^- \leftrightarrow 4OH^-. \quad (4)$$

With the progress of the anodic reaction, the reprecipitation of Cu_2O occurs, which can be explained by the increase of the concentration of $CuCl_2^-$ at the interface between the alloy matrix and the solution enough for the hydrolysis reaction as shown in equation (5) to take place [36].

$$2CuCl_2^- + H_2O \leftrightarrow Cu_2O + 4Cl^- + 2H^+. \quad (5)$$

Cu_2O is thermodynamically unstable and it will be further oxidized to CuO or $Cu_2(OH)_3Cl$ through the reaction of equations (6) - (7):

$$Cu_2O + H_2O \leftrightarrow 2CuO + 2H^+ + 2e^-, \quad (6)$$

$$Cu_2O + Cl^- + 2H_2O \leftrightarrow Cu_2(OH)_3Cl + H^+ + 2e^-, \quad (7)$$

$$2CuO + H{+}{+} + Cl{-}{+} H2O \leftrightarrow Cu2(OH)3Cl. \quad (8)$$

$Cu_2(OH)_3Cl$ is a nonprotective corrosion product, which was proven to be present in the surface layer of the film by the XRD and SEM results. However, CuO in the corrosion product film was not detected in this work. This may have been because, on the one hand, reaction (7) occurs prior to reaction (6) in NaCl solution. Thus, the content of CuO produced by the transformation of Cu_2O is relatively lower than that of $Cu_2(OH)_3Cl$. On the other hand, acidification of Cl^- may also result in the transformation of CuO through equation (8) to $Cu_2(OH)_3Cl$ [16]. The SEM and XRD results indicated that the addition of Y effectively inhibited the transformation of Cu_2O to $Cu_2(OH)_3Cl$, which may have been related to the inhibition effect of Y on the diffusion of Cl^- in the Cu_2O layer.

At this stage, the thickness of the Cu_2O layer of the corrosion product film tended to be stable, and relatively complete corrosion products formed. The diffusion process of O_2 through the corrosion product film to the interface between the film and matrix was hindered. Meanwhile, the electron transport across the film was inhibited, which limited the rate of the cathodic reaction. However, the

anodic dissolution process was not affected. In a freely corroding system, the anodic and cathodic reactions must occur at equal rates [17]. Therefore, another cathodic reaction must occur, for example, the reduction of copper ions to pure copper, as shown in equation (9).

$$CuCl_2^- + e^- \leftrightarrow Cu + 2Cl^-. \quad (9)$$

This chemical reaction process could explain why strong Cu peaks were detected in the XRD results, and it is also consistent with the presence of Cu peaks in the XPS Cu 2p spectra.

With the progress of the corrosion reactions, copper ions and electrons must migrate through the Cu_2O film [44,45]. The rate of corrosion is then limited by the diffusion of these species through the complete layer of Cu_2O. As a result, the growth mode of the Cu_2O film changes from the outward reprecipitation of dissolved copper species to the inward oxidation at a slow rate. From the perspective of lattice defects, the inward oxidation mechanism of the Cu_2O layer is related to Cu_2O being a high-density defective p-type semiconductor, and this mechanism has been reported by Ma [16]. The reaction process can be described in equation(10):

$$4Cu + O_2 \leftrightarrow 2Cu_2O. \quad (10)$$

Compared with the Cu_2O layer formed in the early stage, the Cu_2O layer formed by inward oxidation had a lower defect concentration and was more protective. This may have been related to the slow corrosion rate of the inward oxidation process. It may also be due to some Ni^{2+} entered the Cu_2O lattice to occupy cation vacancies [20].

In XRD profile, there are both paratacamite and botallackite indicated the substitution of Cu^{2+} by Ni^{2+} at some positions. Meanwhile, the XPS results showed that the content of the Ni in the film of the alloy with a Y content of 0.021% was higher than that without Y. Therefore, it can be inferred that Y promoted the diffusion of Ni in the corrosion product film, which is favorable for Ni to enter the Cu_2O lattice and occupy the cation vacancies.

4.2 Analysis of Ni in corrosion product film

The XRD and XPS results showed that the enrichment of Ni occurred in the entire corrosion product film. In the $Cu_2(OH)_3Cl$ layer and the Cu_2O layer formed by the reprecipitation process, Ni element was present in the form of metal Ni, NiO, and $Ni(OH)_2$. In the early corrosion process, while the Cu matrix dissolved and reacted with Cl^-, the Ni matrix also dissolved under the action of Cl^- and formed NiO and $Ni(OH)_2$[36], which can be described by the following reactions:

$$Ni + H_2O + Cl^- \leftrightarrow NiClOH_{ads}^- + H^+ + e^-, \quad (11)$$

$$NiClOH_{ads}^- + Cl^- \leftrightarrow NiCl_2 + OH^- + e^-. \quad (12)$$

$$NiCl_2 + H_2O \leftrightarrow NiO + 2Cl^- + 2H^+, \quad (13)$$

$$NiO + H_2O \leftrightarrow Ni(OH)_2. \quad (14)$$

The metal Ni also exists in the outer and middle layers of corrosion products because the corrosion rate of Ni is two orders of magnitude lower than that of Cu[17].

In the stage of Cu_2O film formation by an inward oxidation mechanism, Cu at the interface between the substrate and film was oxidized in the film, leading to the enrichment of Ni at the interface. Some of the Ni could enter the Cu_2O lattice and occupy the cation vacancies while releasing

electrons, causing electron holes to be annihilated with a higher efficiency than that of Cu [16] and reducing the conductivity of ions and electrons in the film, thereby improving the corrosion resistance of the alloy. With the Ni content incorporated in the Cu_2O lattice increased and its concentration reached a certain value at some local areas, transformation from Cu_2O into amorphous or microcrystalline NiO occurred, which is consistent with the literature results [16]. Thus, a layer of NiO formed at the interface between the matrix and the film. As shown in Table 3, the resistance of the inner layer corrosion product film increased significantly after adding rare earth Y, which may have been due to Y promoting the diffusion of Ni in the Cu_2O layer and accelerating the transformation of the Cu_2O lattice to amorphous or microcrystalline NiO.

4.3 Role of rare earth Y in corrosion

The electrochemical impedance spectra showed that the corrosion resistance of the 90Cu–10Ni alloys first improved and then deteriorated with the increase in the Y content. Reflected in the resistance of the inner film, the effect of Y on the corrosion resistance was more significant. When the content of Y was 0.021%, the resistance was much greater than that of the sample without Y. On the one hand, this was related to the size and number of rare earth inclusions. When the content of Y was less than 0.021%, the effect of Y was dominant in the removal of other impurities in the alloy matrix and the purification of the grain boundary. When the content of Y increased to 0.053%, the size and number of yttrium-rich oxysulfide inclusions increased significantly, which was not conducive to the improvement of the corrosion resistance to a certain extent. On the other hand, the effect of Y on the diffusion of Ni played a key role in the corrosion resistance of the alloy. When the Y content reached 0.021%, it greatly promoted the entry of Ni^{2+} into the Cu_2O lattice, causing NiO to be dominant in improving the corrosion resistance, which explains why the inner film resistance of sample S3 was the largest. As shown in Fig. 13(a), the concentration of cation vacancies and electron holes in the inner Cu_2O formed by inward oxidation of the rare-earth-free alloy was higher, and the number of Ni^{2+} entering the Cu_2O lattice was lower. The incorporation of Ni^{2+} in the lattice defects of Cu_2O could decrease its ionic and electronic conductivity [36]. For the alloys with rare earth additions, Y tended to segregate on the surface of the alloy substrate during the corrosion and reacted with adsorbed O_2 to form rare earth oxide [46], which could promote the entry of Ni^{2+} into the Cu_2O lattice, reducing the concentration of cation vacancies and electron holes in the inner Cu_2O layer and facilitating the transformation of Cu_2O to microcrystalline or amorphous NiO. This process is schematically described in Fig. 13(b).

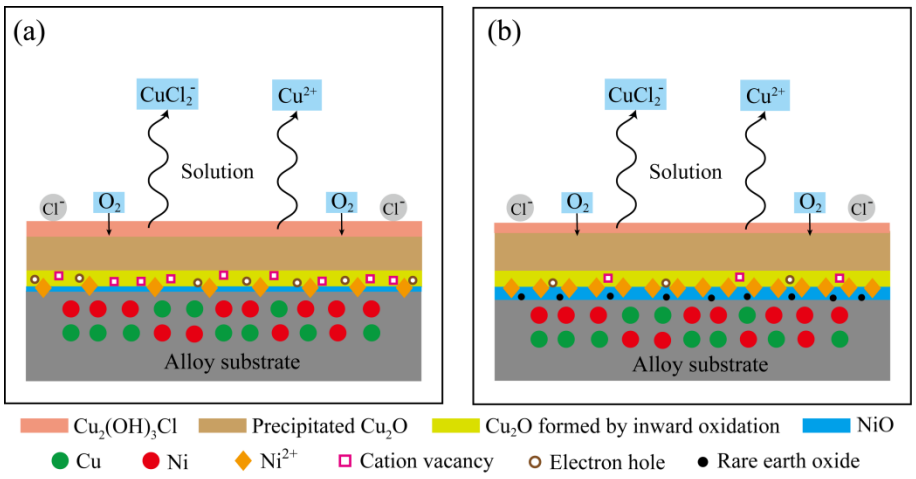

Figure 13. Schematic diagrams for the structure of the corrosion product film on the 90Cu–10Ni alloy after immersion for 30 d in a 3.5% NaCl solution (a) without and (b) with rare earth addition

5. CONCLUSIONS

1) The rare earth Y in the 90Cu–10Ni alloy was mainly in the form of dispersed yttrium-rich oxysulfide inclusions, and the number and sizes of the inclusions increased with the increase in the Y content. A proper amount of Y could refine the secondary dendrite spacing of the as-cast structures.

2) The corrosion product film of the 90Cu–10Ni alloy, which formed by immersion in a 3.5% NaCl solution for 30 d, had a double-layer structure. As the Y content increased, the colors of the corrosion products became darker. When the Y content was 0.021%, the corrosion product film was closely bound to the matrix, and the alloy exhibited the best corrosion resistance, which was attributed to the inhibitory effect of Y on the transformation from Cu_2O to $Cu_2(OH)_3Cl$ and the influence of Y on the diffusion of Ni into the Cu_2O lattice.

3) Y could improve the compactness of the inner corrosion product film, which was beneficial for hindering further corrosion of the matrix. Meanwhile, Y played a key role in improving the corrosion resistance of the alloy by affecting the formation of NiO in the inner corrosion product film.

ACKNOWLEDGMENTS
This project was supported by the National Key Basic Research Program (No. 2016YFB0301400); the Key Research and Development Program of Jiangxi Province (Grant No. 20192ACB50010，20192BBEL50016，20161BBE50065). We thank LetPub (www.letpub.com) for its linguistic assistance during the preparation of this manuscript.

References

1. L. O. Ainara, B. Raquel, J. L. Arana, *Materials*, 12 (2019) 1325.
2. Y. F. Li, C. Y. Ning, *Bioact. Mater.*, 4 (2019) 189.
3. M. A. Khan, S. Sundarrajan, S. Natarajan, *Anti-Corros. Method. Mater.*, 64 (2017) 508.
4. W. H. Xing, X. H. Wang, B. X. Guo, Y. Shao, Y. Y. Wang, *Mater. Corros.*, 69(2018) 1861.
5. H. Nady, M. M. El-Rabiei, M. Samy, *Egypt. J. Pet.*, 26 (2017) 79.
6. X. Z. Zhou, C. P. Deng, Y C. Su, *J. Alloy. Compd.*, 491 (2010) 92.

7. L. Wang, D. C. Kong, C. F. Dong, B. B. Zhao, C. He, Y. Y. Wan, C. Man, X. G. Li, *J. Mater. Eng. Perform.*, 27 (2018) 4280.
8. K. M. Ismail, A. M. Fathi, W. A. Badawy, *Corros. Sci*., 48 (2006) 1912.
9. J. Crousier, A. M. Beccaria, *Mater. Corros.*, 41(1990) 185.
10. X. Y. Mao, F. Fang, J. Q. Jiang, R. S. Tan, *J. Rare Earths*, 27(2009) 1037.
11. G. Y. Lin, W. Yang, Y. C. Wan, P. Tang, B. Wei, S. H. Zhang, *J. Rare Earths*, 27 (2009) 259.
12. Y. Liu, Y. A. Zhang, W. Wang, D. S. Li, J. Y. Ma, J. Du, *Arabian Journal for Science and Engineering*, 43(2018) 6285.
13. X. G. Dong, J. Zhou, Y. Y. Yu, Y. Y. Hu, A. J. Mo, *Journal of Donghua University (English Edition)*, 3 (2013) 249.
14. X. Leng, Y. D. Zhang, Q. Y. Zhou, *Mater. Res. Express*., 5 (2018) 1.
15. R. North, M. Pryor, *Corros. Sci.*, 10 (1970) 297.
16. A. L. Ma, S. L. Jiang, Y. G. Zheng, W. Ke, *Corros. Sci*., 91 (2015) 245.
17. K. Efird, *Corrosion*, 31 (1975) 77.
18. H. H. Li, S. H. Zhang, Y. Chen, M. Cheng, H. W. Song, J. S. Liu, *J. Mater. Eng. Perform.*, 24 (2015) 2857.
19. Z. G. Wang, C. M. Song, Y. H. Zhang, H. Wang, L. Qi, B. Yang, *Mater. Charact.*, 151 (2019) 112.
20. Z. G. Wang, X. Y. Feng, Q. Y. Zhou, H. Wang, Y. H. Zhang, B. Yang, *Corrosion*, 74 (2018) 819.
21. R. C. Chen, Z. G. Wang, F. S. Zhu, H. J. Zhao, J. Qin, L. Q. Zhong, *J. Alloy. Compd.*, 824 (2020) 153849.
22. X. Y. Mao, F. Fang, J. Q. Jiang, R. S. Tan, *Rare Metals*, 28 (2009) 590.
23. O. O. Ekerenam, A. L. Ma, Y. G. Zheng, W. Emori, *J. Mater. Eng. Perform*., 26 (2017) 1701.
24. S. B. Hu, L. Liu, Y. Cui, Y. Li, F. H. Wang, *Corros. Sci*., 146 (2019) 202.
25. A. M. Beccaria, J. Crousier, *Brit. Corros. J.*, 24 (1989) 49.
26. F. Mansfeld, G. Liu, H. Xiao, C. H. Tsai, B. J. Little, *Corros. Sci*., 36 (1994) 2063.
27. R.L. Frost, *Spectrochim. Acta A*, 59 (2003) 1195.
28. L. Babouri, K. Belmokre, A. Abdelouas, *Int. J. Electrochem. Sci.*, 10 (2015) 7818.
29. K. Chandra, V. Kain, G. K. Dey, P.S. Shetty, R. Kishan, *Eng. Fail. Anal.*, 17 (2010) 587.
30. B. Sun, T. Y. Ye, Q. Feng, J. H. Yao, M. M. Wei, *Materials*, 8(2015) 6029.
31. I. Milosev, M. Metikos-Hukovic, *J. Appl. Electrochem*., 29 (1999) 393.
32. H. Nady, N.H. Helal, M.M. El-Rabiee, W.A. Badawy, *Mater. Chem. Phys.*, 134 (2012) 945.
33. S. Colin, E. Beche, R. Berjoan, H. Jolibois, A. Chambaudet, *Corros. Sci*., 41 (1999) 1051.
34. W. A. Badawy, M. M. El-Rabiee, N. H. Helal, *Electrochem. Acta*, 56 (2011) 913.
35. K. M. Ismail, W. A. Badawy, *J. Appl. Electrochem.*, 30(2000) 1303.
36. W.A. Badawy, K.M. Ismail, A.M. Fathi, *Electrochem. Acta*, 50 (2005) 3603.
37. J. Zhang, W. Zhang, C. Yan, K. Du, F. Wang, *Electrochem. Acta*, 55 (2009) 560.
38. Y. H. Zhang, X. Y. Feng, C. M. Song, *MRS Commun.*, (2018) 1.
39. R. W. Zhang, Z. Y. Zhu, X. Leng, *Int. J. Electrochem. Sci.*, 13(2018) 11526.
40. S.Ld. Assis, S. Wolynec, I. Costa, *Electrochem. Acta*, 51 (2006) 1815.
41. G. Kear, B. Barker, K. Stokes, F. Walsh, *J. Appl. Electrochem*., 34 (2004) 659.
42. M. Metiko-Hukovi, R. Babi, I. Kugor, *Corros. Sci*., 53 (2011) 347.
43. J. Mathiyarasu, N. Palaniswamy, V. S. Muralidharan, *J. Chem. Sci.*, (1999) 377.
44. G. Bianchi, P. Longhi, *Corros. Sci.*, 13 (1973) 853.
45. S.A. Campbell, G.J.W. Radford, C.D.S. Tuck, *Corrosion*, 58 (2002) 57.
46. I. Milošev, M. Metikoš-Huković, *Electrochem. Acta*, 42 (1997) 1537.